metals

MDPI

Article

Development of Novel Mg-Al-Mn-Based Alloys with High-Strength and Ductility via Co-Addition of Ce and Ca

Wei Liu, Shuo Li, Hucheng Pan *, Yuan Zhang, Zhen Pan, Sen Wang, Yuping Ren and Gaowu Qin

Key Laboratory for Anisotropy and Texture of Materials (Ministry of Education), College of Materials Science and Engineering, Northeastern University, Shenyang 110819, China; 2370462@stu.neu.edu.cn (W.L.); 2370438@stu.neu.edu.cn (S.L.); 2270625@stu.neu.edu.cn (Y.Z.); 2410201@stu.neu.edu.cn (Z.P.); 2210227@stu.neu.edu.cn (S.W.); renyp@atm.neu.edu.cn (Y.R.); qingw@smm.neu.edu.cn (G.Q.)
* Correspondence: panhc@atm.neu.edu.cn

Abstract: In this work, the novel Mg-Al-Mn-Ce-(Ca) alloy system has been developed, and large-scaled and thin-walled Mg alloy extruded profiles with an actual composition of Mg-8Al-0.57Mn-0.42Ce (AM80E), and Mg-8Al-0.57Mn-0.42Ce-0.31Ca (AM80EA) were successfully fabricated. The extruded AM80EA alloy profile exhibited a refined recrystallized grain structure (with an average size of ~6.96 μm) and high-density second phase. These abundant micro-nano precipitates effectively inhibited grain boundary migration during recrystallization, achieving obvious grain refinement and providing strong grain refinement strengthening effects. Concurrently, these high-density second-phase particles can also prevent dislocations from slipping. The fine-grain strengthening and second-phase strengthening contribute to the yield strength (YS) of ~174 MPa, the ultimate tensile strength (UTS) of ~309 MPa, and the elongation (EL) of ~13.7% of the AM80E alloy profile. Through the further addition of the Ca element, the AM80EA alloy achieves better comprehensive mechanical properties than the AM80E alloy, exhibiting a YS of ~193 MPa, UTS of ~346 MPa, and EL of ~16.5%. This study demonstrates that, through rational alloying design and extrusion process control, Mg-Al-Mn-Ce-(Ca)-based alloy profiles with excellent mechanical properties can be obtained. Relevant work would provide references for developing these cost-effective high-strength Mg alloy products and promote their industrial applications.

Keywords: Mg wrought alloys; large-sized profile; dynamic recrystallization; grain refinement; mechanical properties

check for updates

Academic Editors: Umberto Prisco and Frank Czerwinski

Received: 21 February 2025
Revised: 8 March 2025
Accepted: 21 March 2025
Published: 25 March 2025

Citation: Liu, W.; Li, S.; Pan, H.; Zhang, Y.; Pan, Z.; Wang, S.; Ren, Y.; Qin, G. Development of Novel Mg-Al-Mn-Based Alloys with High-Strength and Ductility via Co-Addition of Ce and Ca. *Metals* **2025**, *15*, 361. https://doi.org/10.3390/met15040361

Copyright: © 2025 by the authors. Licensee MDPI, Basel, Switzerland. This article is an open access article distributed under the terms and conditions of the Creative Commons Attribution (CC BY) license (https://creativecommons.org/licenses/by/4.0/).

1. Introduction

The increasing urgency of climate change and energy sustainability has driven a growing demand for new-energy vehicles and high-speed railway systems. A major challenge in this field is in developing advanced lightweight structural materials [1]. Magnesium (Mg) alloys, as the lightest structural metallic materials available, offer intrinsic advantages for weight reduction. Consequently, developing high-performance, large-scale, and complex extruded Mg alloy profiles has become a critical research focus, especially for new-energy vehicles [2–4]. However, the broader application of Mg alloys is constrained by their inherently low strength and limited plasticity at ambient temperatures, particularly in the fabrication of extruded profiles. To address this problem, this work aims to develop large-scaled and thin-walled wrought Mg alloy profiles with improved mechanical properties via compositional optimization.

Alloying is a widely adopted strategy for enhancing the mechanical properties of Mg alloys, and rare-earth (RE) elements such as Gd and Y play crucial roles in refining their grain structures and improving their deformation behavior [5–7]. However, for industrial applications of Mg products, reducing the total cost remains a key factor. Light rare-earth (LRE) elements, such as cerium (Ce) and samarium (Sm), have attracted increasing attention due to their ability to strengthen Mg alloys while maintaining a low density and reducing production costs [8–10]. Ce, as a representative LRE element, has been recently utilized for microstructural optimization in Mg alloys. For example, Li et al. [11] reported that Ce addition significantly inhibits recrystallization and refines grains in Mg alloys, increasing the UTS value from 120 MPa of pure Mg to 352 MPa of Mg-0.3Ce alloy. Similarly, Xie et al. [12] demonstrated that co-addition of Ce and Sm in Mg-Sm-Ce alloys resulted in a high YS of ~372 MPa in the extruded samples, which remained as high as ~275 MPa at an elevated temperature of 250 °C.

In addition to RE elements, the calcium (Ca) element is frequently introduced into Mg alloys to tailor their microstructure and mechanical properties, particularly in commercial Mg alloys [13–15]. Pan et al. [16] found that Ca additions in Mg-Sn-Ca alloys promote segregation at low-angle grain boundaries (LAGBs), leading to the formation of ultrafine grains (~0.32 μm) and achieving a remarkable YS of ~440 MPa in Mg-2Sn-2Ca alloys. Zhang et al. [17] investigated the influence of trace Ca additions in Mg-1Mn-0.5Al alloys, and found that the Al_2Ca phases would contribute to the grain refinement, and thus improved the alloys' mechanical properties after extrusion. In particular, Mg-Al-Zn and Mg-Al-Mn series alloys are widely used among the commercially available Mg systems. Therefore, in order to utilize the advantages of Ce and Ca elements, this study designed Mg-8Al-0.57Mn-0.42Ce-(0.31Ca) alloys for complex-profile extrusion based on commercial AM80 alloys. The additions of Ce and Ca effectively enhanced the formability and mechanical properties of the AM80-based alloy. After extrusion processing at 375–385 °C, large-scale and thin-walled extruded Mg profiles with high surface quality were successfully fabricated. The as-extruded alloys exhibited well-balanced mechanical properties, including a YS of ~193 MPa, UTS of ~356 MPa, and EL of ~16.5%.

2. Materials and Methods

The Mg alloy billets were melted in a vacuum induction furnace using pure Mg (99.99 wt.%), pure Ce (99.99 wt.%), pure Al (99.99 wt.%), Mg-20Ca master alloy, and Mg-30Mn master alloy, and as-cast ingots with a diameter of 178 mm were produced. Two samples were prepared, including Mg-8Al-0.57Mn-0.42Ce (wt.%) and Mg-8Al-0.57Mn-0.42Ce-0.31Ca (wt.%) alloys, which were named the AM80E and AM80EA alloys, respectively. The cast billets were homogenized in an electric furnace at 410 °C for 20 h. After the homogenization treatment, the Mg ingots were machined into cylinder billets 178 mm in diameter and were then extruded at 380 °C, with an extrusion ratio of 28:1 and extrusion rate of 0.6 mm/s. The nomenclature, composition, and extrusion parameters of the above Mg-Al-Mn-Ce-(Ca) alloys are shown in Table 1. Figure 1 shows the extruded profiles obtained from the experiments in this paper.

Table 1. The extrusion parameters of AM80E and AM80EA alloys.

Samples	Alloy Composition, wt.%	Extrusion Temperature, °C	Extrusion Rate, mm/s
AM80E	Mg-8Al-0.57Mn-0.42Ce	375–385	0.6
AM80EA	Mg-8Al-0.57Mn-0.42Ce-0.31Ca	375–385	0.6

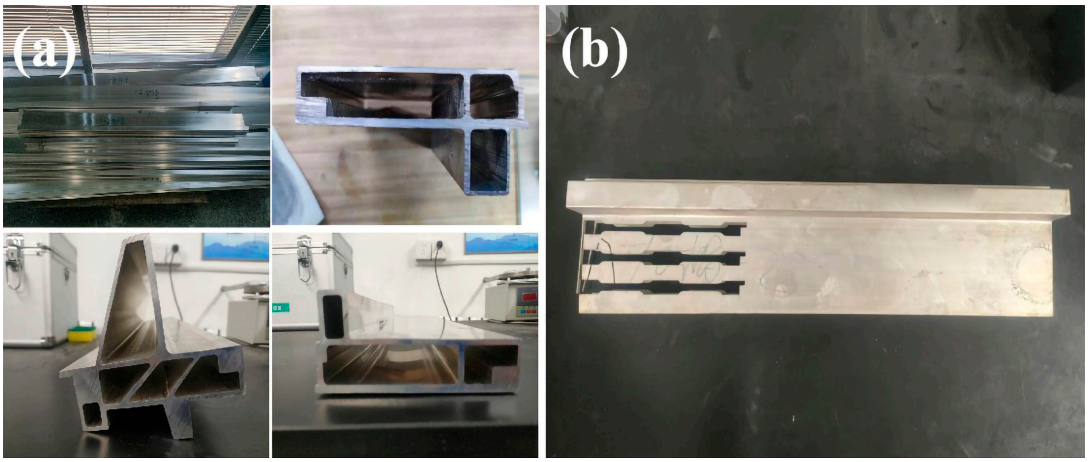

Figure 1. Images of extruded AM80E and AM80EA alloy profiles. (**a**) The shapes of the extruded AM80E; (**b**) the shape of the tensile samples.

The tensile tests were conducted on plate specimens (as shown in Figure 2) along the extrusion direction (ED) at room temperature, using an AG-X plus 100 KN testing machine (Shimadzu Corporation, Kyoto, Japan) with a tensile rate of 0.001 s^{-1}. The microstructure was characterized using optical microscopy (OM, Olympus OLS3100, Olympus, Tokyo, Japan) and scanning electron microscopy (SEM, JEOL JSM-7001F, JEOL, Tokyo, Japan) with an electron backscatter diffraction (EBSD) detector. Both the OM and SEM specimens were finely polished, followed by etching in a solution of 20 mL acetic acid, 3 g picric acid, 20 mL water, and 50 mL ethanol. EBSD samples were prepared by mechanical polishing and subsequent argon ion polishing. The EBSD data were analyzed using AZtec Crystal software (Version 2.1.2). Transmission electron microscopy (TEM) (Thermo Fisher Scientific, Waltham, MA, USA) observations were conducted with an acceleration voltage of 200 kV (JEM-2100F, JEOL). The thin foils for TEM observations were mechanically polished to ~40 μm and then ion-milled by a GATAN PIPS691, (GATAN, Pleasanton, CA, USA).

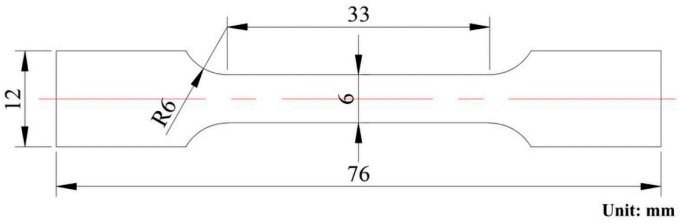

Figure 2. Diagram of tensile specimen.

3. Results

3.1. Mechanical Properties of As-Extruded Mg Alloys

The engineering stress–strain curves of the as-extruded AM80E and AM80EA alloys are shown in Figure 3, and Table 2 summarizes their corresponding mechanical properties. The AM80E alloy exhibits a YS of ~174 MPa, a UTS of ~309 MPa, and a high EL of ~13.7%. After the addition of the Ca element, the YS increases from ~174 MPa to ~193 MPa, while the UTS reaches 346 MPa, with a notable EL of 16.5%. These results indicate that trace Ca addition significantly enhances the mechanical properties of the AM80EA alloy. To further demonstrate the novelty of the present AM80EA alloy, previously reported Mg-Al and/or Mg-Al-Mn based alloys were reviewed [18–26], and Figure 4 shows the comparison of the mechanical properties between some related studies and the present Mg sample. The poorer mechanical properties of previous Mg-Al based samples can be contributed to

their lower Al content, insufficient addition of rare earth elements, or lack of multi-element synergistic optimization.

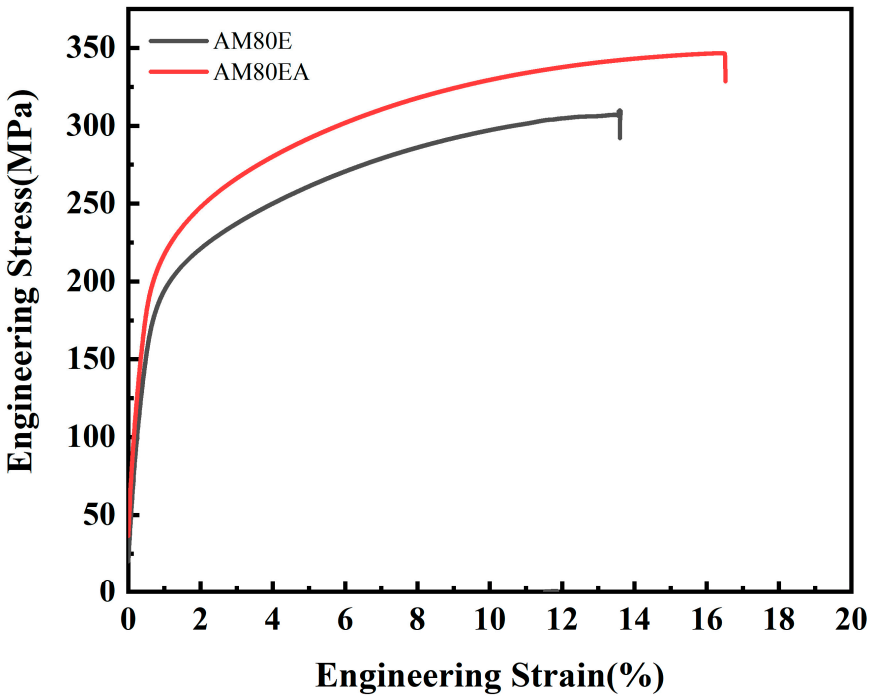

Figure 3. Engineering stress–strain curves of as-extruded AM80E and AM80EA alloys.

Table 2. Mechanical properties of the extruded profiles of the AM80E and AM80EA alloys.

Samples	YS/MPa	UTS/MPa	EL/%
AM80E	174 ± 3	309 ± 2	13.7 ± 0.5
AM80EA	190 ± 5	346 ± 5	16.5 ± 1

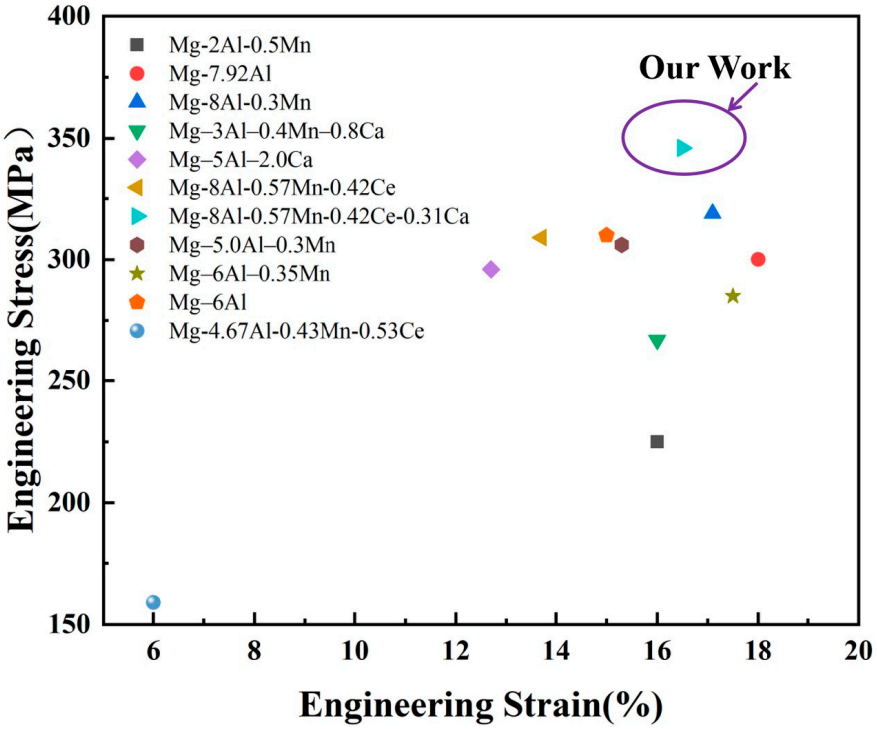

Figure 4. Plot of tensile strength and elongation of the reported extruded Mg-Al-Mn alloys.

3.2. Microstructures of As-Extruded Mg Alloys

3.2.1. OM and SEM Images of As-Extruded Mg Alloys

The optical microstructures of the as-extruded AM80E and AM80EA alloys are shown in Figure 5. The AM80E alloy exhibits a high recrystallization fraction, with an average grain size of 12.5 μm (Figure 5a,c). In contrast, the AM80EA alloy shows a lower recrystallization fraction and finer grain size, with an average recrystallized grain size of 6.72 μm in Image J software 1.53c (Figure 5b,d). The above results show that with the addition of the Ca element, the recrystallization grain size of the alloy decreases. The grain refinement in the AM80EA alloy is attributed to the segregation and enrichment of high-density second phase precipitates at the grain boundaries, which inhibit recrystallized grain growth.

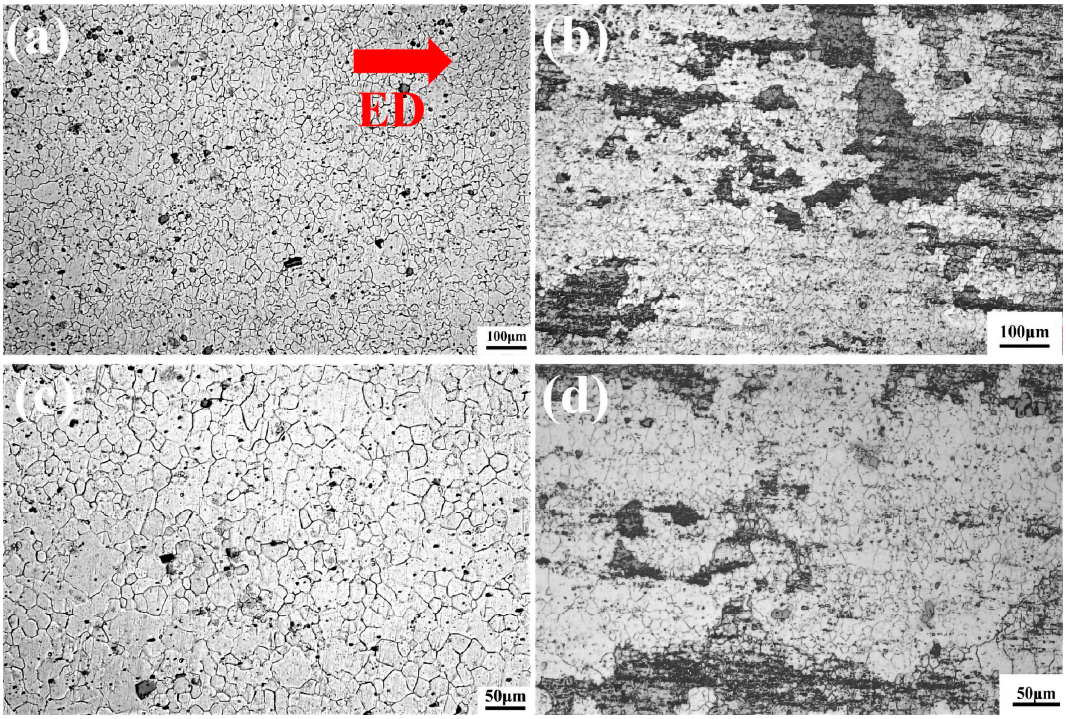

Figure 5. Optical microscopy of images of as-extruded (**a**,**c**) AM80E alloy; (**b**,**d**) AM80EA alloy.

The SEM images and corresponding EDS results of the AM80E alloy are shown in Figure 6. Figure 6a presents a low-magnification SEM image of the alloy, where the ED direction is the extrusion direction of the alloy. In Figure 6a, a large number of micrometer-sized second phases can be found along the extrusion direction. A higher-magnification SEM image is displayed in Figure 6b, revealing that the second-phase particles mainly exist in two forms: large blocky particles and fine granular particles dispersed in the matrix. To determine the composition of these second-phase particles, an EDS analysis was conducted, and the results are shown in Figure 6c. The analysis reveals that the large-sized blocky second phase is mainly an Al-Mn phase. In addition, some fine-dispersed Al-Ce phases are also present within the alloy. Figure 6d,e shows the point scanning results for point A and B in Figure 6b, further confirming that the large-size second phase particles are mainly Al-Mn phases. Meanwhile, the point scanning at point C, presented in Figure 6f, indicates that the proportions of Al and Ce are 17.20% and 22.28%, respectively, suggesting that the fine granular second-phase particles correspond to the Al-Ce phase.

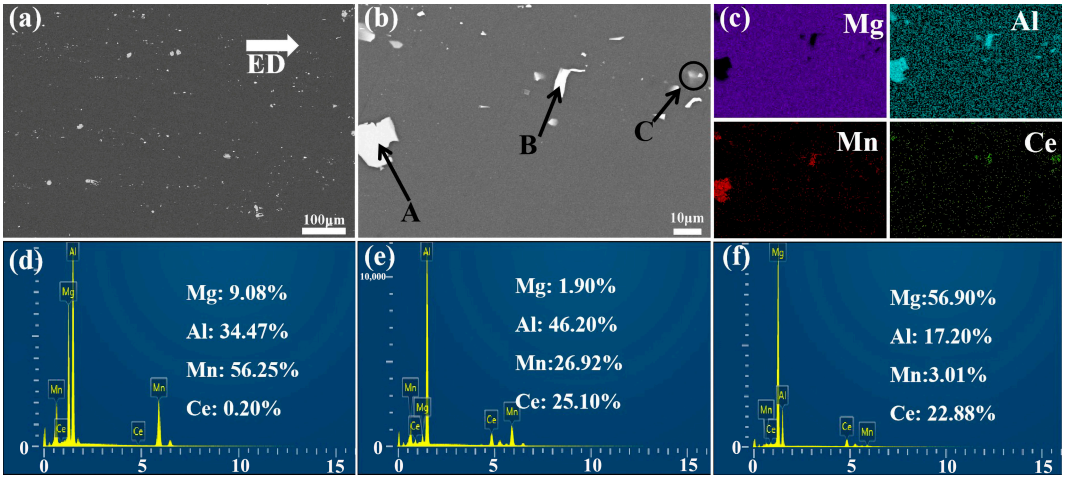

Figure 6. Backscattered SEM images and the corresponding EDS results of the as-extruded AM80E alloy. (**a**,**b**) Low- and high-magnification SEM images; (**c**) map scanning results corresponding to (**b**); (**d**–**f**) Point-scanning results corresponding to points A, B, and C in (**b**).

Figure 7 shows the SEM images and the corresponding EDS results of the as-extruded AM80EA alloy. As shown in Figure 7a,b, the bulk micron-sized second-phase particles broke up during the extrusion process and are redistributed in a streamlined pattern along the ED, exhibiting a bright contrast in the SEM images. In addition to these larger blocky second-phase particles, second-phase particles with smaller sizes are also observed, dispersed throughout the alloy matrix. To further determine the elemental composition of these phases, an EDS analysis was performed on the regions shown in Figure 7c,d. The results show that most of the bulk micron-sized second phases are mainly Al-Mn phases. Furthermore, as shown in Figure 7d, an aggregation of Ca is detected in the lower right corner of the scanned region, suggesting the presence of Ca-containing particles or Al-Ca phases. Figure 7e,f are the point scan results of the second phase at points A and B in Figure 7b. It can be seen that the larger blocky second phase at point A is mainly an Al-Mn phase, and the fine granular second phase at point B has a higher Al and Ca content, which can be inferred as an Al-Ca phase.

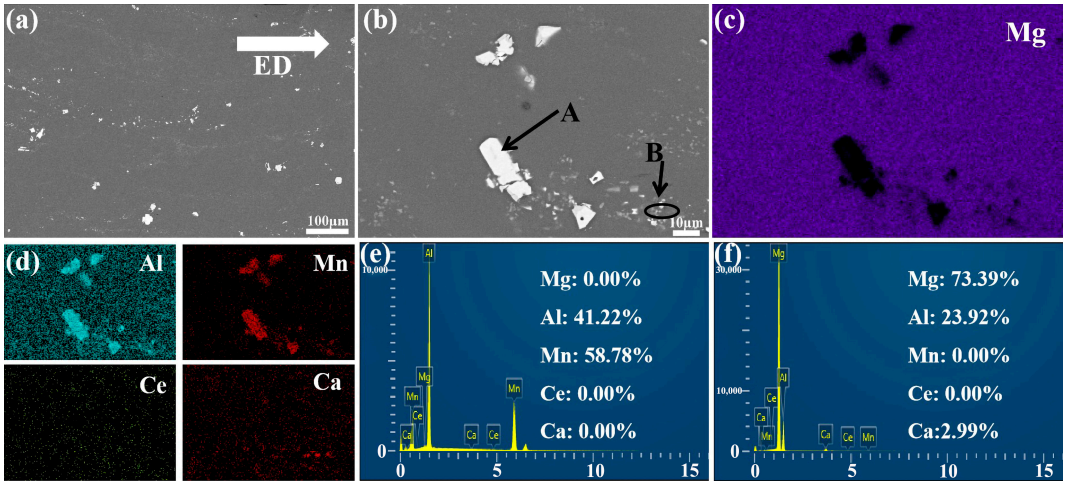

Figure 7. Backscattered SEM images and the corresponding EDS results of the as-extruded AM80EA alloy. (**a**,**b**) Low-and high-magnification SEM images; (**c**,**d**) Map scanning results corresponding to (**b**); (**e**,**f**) Point-scanning results corresponding to points A, B in (**b**).

3.2.2. XRD Results of As-Extruded Alloys

Figure 8 shows the XRD patterns of the AM80E and AM80EA alloys. As shown in Figure 8a, the formed Al-Mn phase in the AM80E alloy can be determined to be the Al_8Mn_5 phase. In addition to the Al-Mn phase, many diffraction peaks of the Al-Ce phase were also observed in the AM80E alloy. Thus, it can be determined that the main second phase in the AM80E alloy is the Al_8Mn_5 and the Al-Ce phase. For the AM80EA alloy (Figure 8b), diffraction peaks for the Al_2Ca phases can be detected; thus, the major second phases should belong to the Al_8Mn_5 and Al_2Ca phases in the AM80EA alloy with the addition of the Ca element.

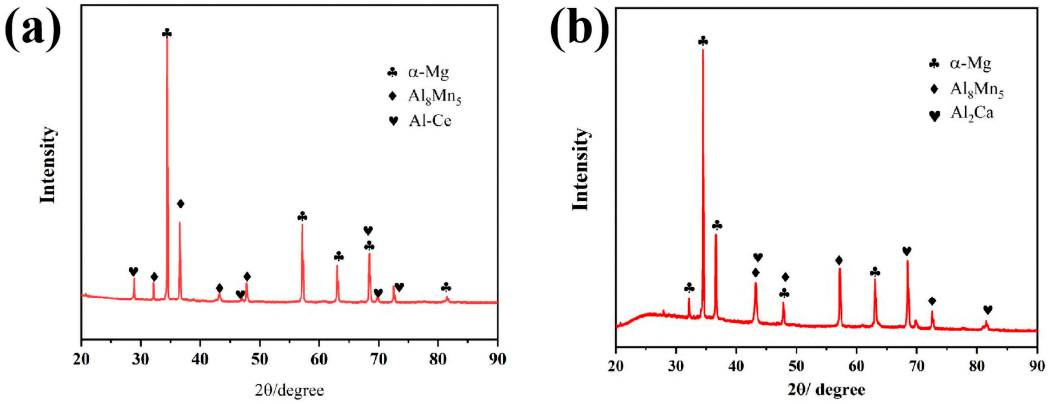

Figure 8. XRD patterns of as-extruded (**a**) AM80E and (**b**) AM80EA alloys.

3.2.3. EBSD Results of As-Extruded Alloys

Figure 9 presents the EBSD results of the AM80E alloy. The results indicate that the as-extruded AM80E alloy exhibits a completely DRXed microstructure, characterized by a relatively uniform grain size. The average grain size, as measured from Figure 9a, is estimated to be 13.82 μm (as shown in Figure 9d). Due to the significant frictional heat generated during the extrusion of large-sized profiles, grain coarsening is typically expected. However, the AM80E alloy maintains a relatively fine grain structure, which plays a crucial role in its high strength. The fraction of LAGBs in the AM80E alloy is relatively low, accounting for only 8.15% as determined by AZtec Crystal software (Version 2.1.2), as shown in Figure 9b. Figure 9c presents the kernel average misorientation (KAM) map, revealing a low residual dislocation density within the grains, with an average KAM value of 0.34°. The texture analysis in Figure 9e,f shows that the alloy develops a distinct <0001> basal texture, with a maximum texture intensity of 9.57 mrd.

Figure 10 presents the EBSD results of the AM80EA alloy. Unlike the AM80E alloy, the AM80EA alloy exhibits a bimodal grain structure, consisting of a mixture of large un-DRXed grains and fine DRXed grains. The average grain size is 6.96 μm, which is significantly smaller than that of the AM80E alloy (Figure 10d). This grain refinement is likely attributed to the presence of a high density of dispersed second-phase particles, which hinder grain boundary migration during extrusion, thereby restricting grain growth. Therefore, the significant grain refinement in the AM80EA alloy is a primary factor contributing to its superior YS compared to the AM80E alloy. Statistical analysis reveals that the proportion of LAGBs in the AM80EA alloy is 15.9% (Figure 10b), which is slightly higher than that of the AM80E alloy. Additionally, the average KAM value remains 0.34° (as shown in Figure 10c), indicating that the extrusion process does not introduce a substantial number of residual dislocations in the AM80EA alloy, which can be attributed to the relatively high extrusion temperature. From Figure 10e,f, it can be revealed that the alloy exhibits a distinct <0001> texture with a maximum texture intensity of 12.57 mrd, which is slightly higher than that of the AM80E alloy.

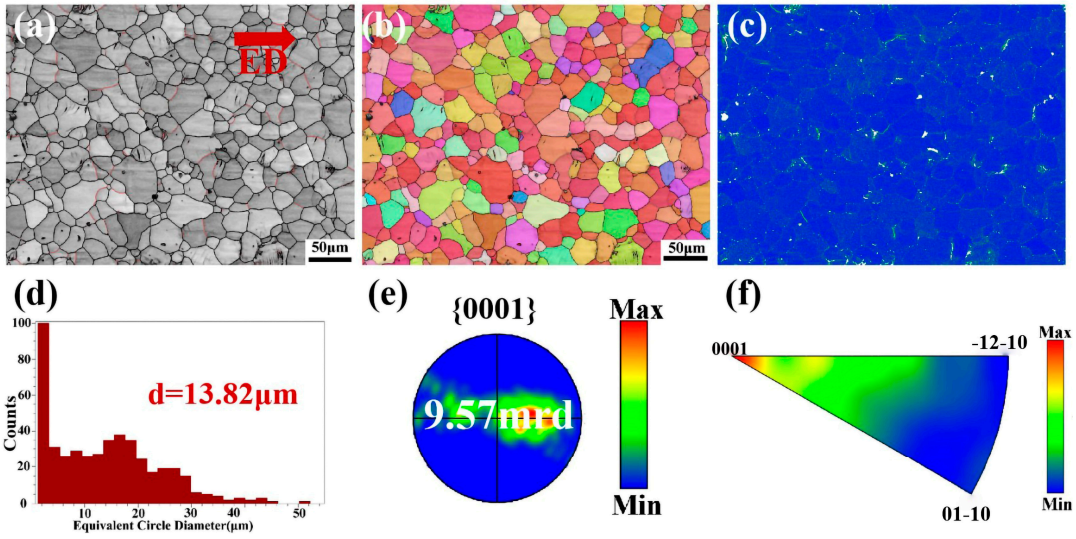

Figure 9. EBSD results of the as-extruded AM80E alloy. (**a**) BC+GB map; (**b**) Inverse pole figure (IPF) map; (**c**) Kernel average misorientation (KAM) map; (**d**) Histogram of grain size; (**e**) Pole figure (PF); (**f**) Inverse pole figure (IPF).

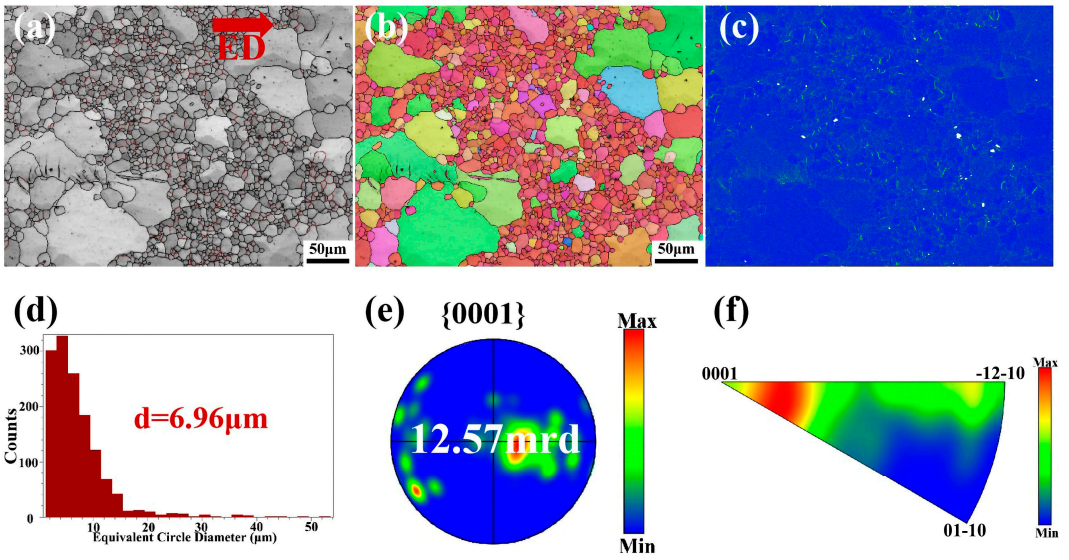

Figure 10. EBSD results of the as-extruded AM80EA alloy. (**a**) BC+GB map; (**b**) IPF map; (**c**) KAM map; (**d**) Histogram of grain size; (**e**) PF; (**f**) IPF.

3.2.4. TEM Analysis of As-Extruded Alloys

To further understand the composition, content, and distribution of second phases in the extruded AM80E and AM80EA alloys, as well as the interaction mechanisms between these phases, grain boundaries, and residual dislocations, TEM characterization was carried out. Figure 11 shows the TEM images of the AM80E alloy. As can be seen from Figure 11b, a large number of nano-phases are dispersedly distributed within the alloy as indicated by the red circle. Figure 11c,d clearly illustrates that these nano-precipitates interact with dislocations. These nano-precipitates pin the dislocations, leading to the pile-up and aggregation of dislocations. According to the Orowan mechanism, these second-phase particles hinder dislocation motion, thereby significantly enhancing the alloy's strength [27,28]. Two primary types of nano-precipitates are observed in the AM80E alloy: particulate and blocky phases. To further determine their composition, an EDS analysis was performed and the results are shown in Figure 11f,h. The results indicate that the blocky phases are primarily composed of Al-Mn and Al-Ce phases. In addition to their role

in dislocation slipping, these second-phase particles also hinder grain boundary migration, contributing to grain refinement and improving mechanical properties.

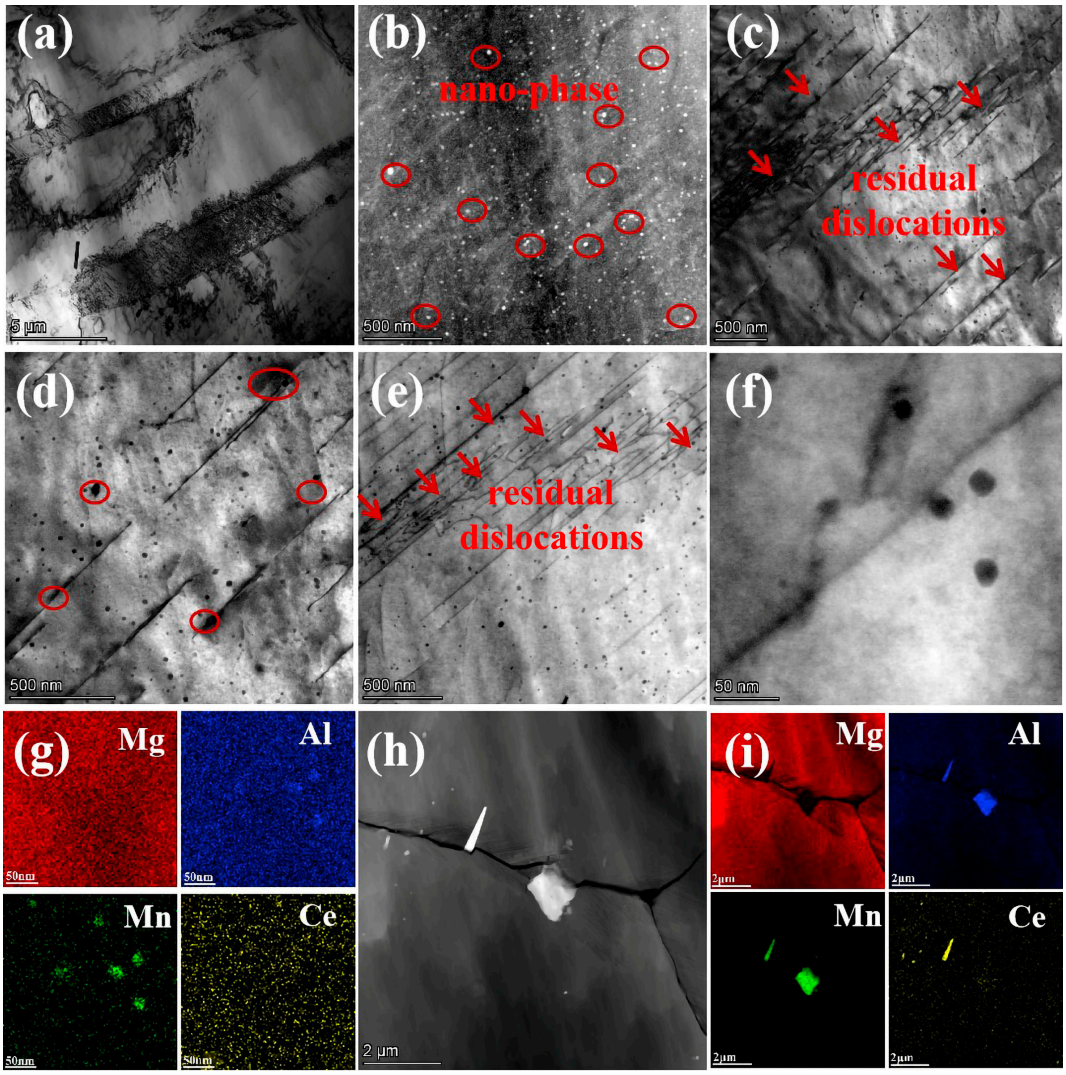

Figure 11. TEM images and EDS results of as-extruded AM80E alloy. (**a**) TEM image of AM80E alloy; (**b**,**d**) Nano-phases in AM80E alloy; (**c**,**e**) Residual dislocations in AM80E alloy; (**f**,**g**) Particulate nano-phases and corresponding EDS results; (**h**,**i**) Blocky micro-phase and corresponding EDS results.

Figure 12 shows the TEM images of AM80EA alloy. As can be seen from Figure 12a,b, a large number of nano-phases are uniformly distributed in the AM80EA alloy, as indicated by the red circle. Interactions between dislocations and nano-precipitated phases can be found, as shown in Figure 12b. Figure 12c shows a fine grain of the AM80EA alloy, where a high density of residual dislocations can be found inside the alloy matrix. According to the high-magnification image of the grain in Figure 12d, it is clear that the nano-phases formed inside the alloy can effectively hinder dislocation slipping, and thus, high-density residual dislocations can be obtained. Therefore, the nano-second phases uniformly distributed inside the alloy at the intra-grain and grain boundaries would increase the strength of the alloy by hindering dislocation slip through the Orowan mechanism. In addition, the precipitation of these nano-precipitated phases, especially the second phase at the grain boundaries, will obviously hinder the boundaries' migration and thus refine the alloy grains. For example, in Figure 12e,f, the high density of gray nano-precipitated phases and brighter micron-sized phases are distributed at the grain boundaries.

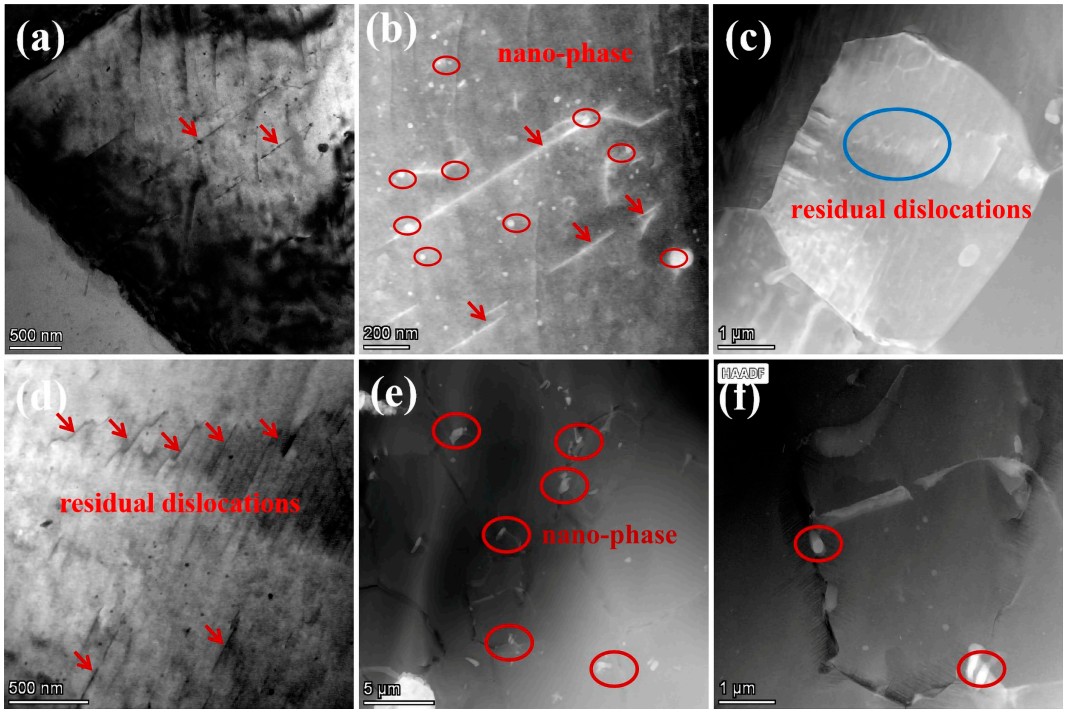

Figure 12. TEM images of as-extruded AM80EA alloy. (**a**) TEM image of AM80EA alloy; (**b**,**c**) Nano-phases in AM80EA alloy; (**d**) DF-STEM image of AM80EA alloy and residual dislocations within the grain in AM80EA alloy; (**e**,**f**) Fine grains and second phase at grain boundaries in AM80EA alloy.

Figure 13 shows the distribution of the second phase of the AM80EA alloy and the corresponding EDS results. From Figure 13a,b, it can be observed that besides some spherical and bulk second phases, there are also some second phases with finer-size and diffuse distribution. As shown in Figure 13c, second-phase particles of various scales are distributed both at the grain boundaries and within the grains. To further determine the elemental compositions of these nano-phases, EDS was employed for their analysis. The results of Figure 13d confirm the presence of Al-Mn and Al-Mn-Ce phases, along with a substantial number of Al-Ca phases. The Al-Ca phases play a dual role in enhancing the mechanical properties of the alloy. Firstly, these fine, densely distributed particles effectively impede dislocation motion, thereby strengthening the alloy through the Orowan mechanism. Secondly, they hinder grain boundary migration, leading to significant grain refinement, which further contributes to the improvement of mechanical strength.

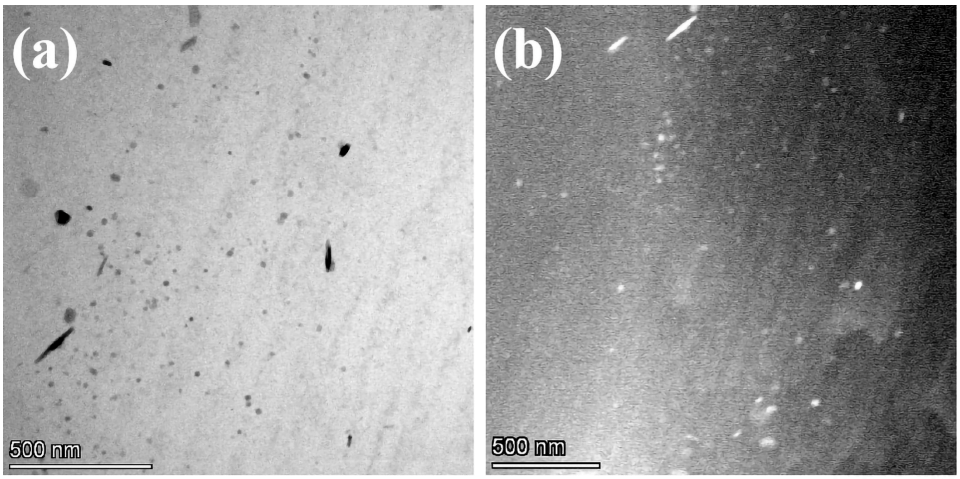

Figure 13. *Cont.*

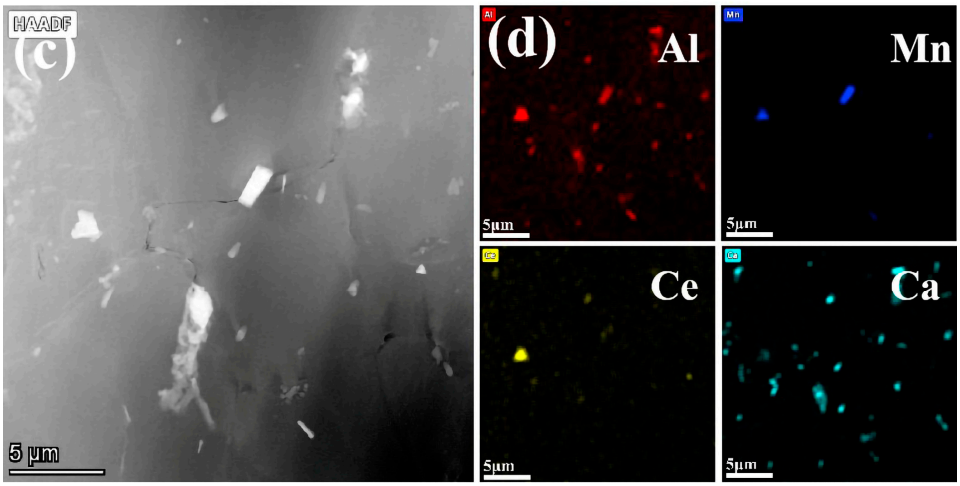

Figure 13. The nano-phase corresponding EDS results and of as-extruded AM80EA alloy. (**a**) TEM image of nano-phases; (**b**) DF-STEM image of nano-phases; (**c**,**d**) HAADDF-STEM image of nano-phases and corresponding EDS results.

4. Discussion

With the addition of Ca and Ce, both AM80E and AM80EA alloys exhibit excellent mechanical properties. In particular, the AM80EA alloy achieves an outstanding balance of strength and ductility, with a YS of ~190 MPa, a UTS of ~346 MPa, and an EL of ~16.5%, even in large-size extruded profiles. It is well known that the processing and deformation of large-size magnesium alloy profiles require higher processing temperatures, and higher processing temperatures will inevitably be accompanied by the growth of alloy grains. This occurs due to the much higher migration rate of new DRX grain boundaries at elevated temperatures. Migration and diffusion rates exhibit exponential growth with increasing temperatures, leading to the coarsening of the alloy grains. However, the extruded profiles of the AM80EA alloy prepared by the co-addition of Ce and Ca not only exhibit a bimodal grain structure but also have a finer average grain size than that of the AM80E alloy. Comparing the AM80E and AM80EA alloys, it can be clearly appreciated that a large number of dense Al-Ca nano-phases are dynamically precipitated in the AM80EA alloy with the addition of Ca. The existence of these Al-Ca nano-phases significantly affects the microstructure evolution of the AM80EA alloy. On the one hand, the precipitation of high-density micron-sized Al-Mn phases provides nucleation sites for the alloy during the recrystallization process, which promotes the recrystallization behavior of the alloy. Furthermore, the dynamically precipitated Al-Ca phases at the grain boundaries hinder the migration of the grain boundaries and thus refine the grain size of the alloy. On the other hand, the dispersed precipitation of the Al-Ca phase also interacts with dislocations, thus hindering the slip of dislocations and inducing the Orowan mechanism to improve the strength of the alloys.

Despite the high processing temperature, both the AM80E and AM80EA alloys maintained relatively fine grain sizes—particularly the AM80EA alloy, where the average grain size remained at 6.96 μm. According to the Hall–Petch relationship:

$$\sigma_y = \sigma_0 + kd^{-1/2} \quad (1)$$

where σ_y is the yield stress, σ_0 is the friction stress, d is the average grain size, and k is the stress concentration coefficient, it can be found that the YS of the alloy is inversely proportional to the average grain size [29,30]. The decreased grain size from 13.82 μm in AM80E to 6.96 μm in AM80EA can thus lead to an increase in YS values. In addition,

when σ_0 and k are adopted as ~50 MPa and ~200 MPa·μm$^{1/2}$ [31], the the grain boundary strengthening contribution of the AM80E alloy and AM80EA alloy can be calculated as ~103 MPa and ~125 MPa, respectively. Experimental results confirm that a reduction in grain size leads to a significant increase in yield strength. Since the AM80EA alloy exhibits a finer average grain size than that of the AM80E alloy, the grain refinement strengthening is likely the dominant factor contributing to its high YS value.

Additionally, the higher density of dynamically precipitated phases in the AM80EA alloy further enhances its mechanical strength. As revealed by SEM images, the AM80EA alloy contains a greater volume fraction of second-phase precipitates. These precipitates play a crucial role in strengthening the alloy by inhibiting grain boundary migration. Specifically, the nano-sized Al_2Ca phases would effectively pin dislocations and restrict the growth of the recrystallized grains [32,33]. Furthermore, the random orientation of fine recrystallized grains improves plasticity. The precipitation of the nano second phase will pin dislocations inside the alloy, thus further increasing the strength of the alloy through the Orowan mechanism. The critical resolved shear stress (CRSS) required for the dislocations to bypass the particles of the precipitated phase can be calculated by the following equation [34]:

$$\Delta\tau_{Orowan} = \frac{Gb}{2\pi\sqrt{1-v}}\left(\frac{1}{\lambda}\right)ln\left(\frac{D_p}{r_0}\right) \quad (2)$$

where $\Delta\tau_{Orowan}$ is the increase in the CRSS of the selected slip system due to precipitation strengthening, G is the shear modulus (~17 GPa), b the Burgers vector of dislocation (~0.32 nm), ν the Poisson ratio (~0.3), λ the effective planar inter-particle spacing, D_P the mean planar diameter of the precipitate, and r_0 the core radius of dislocation, which is conveniently assumed as b (~0.32 nm) in this work. From this equation, it is evident that the smaller second-phase precipitates with higher density can provide a stronger Orowan strengthening effect in Mg alloys. For the AM80EA alloy, the values of λ~300 nm and D_P~50 nm are adopted (Figure 13), and the increase in the stress can be calculated to be ~72 MPa. The fine, uniformly dispersed second-phase particles in the AM80EA alloy matrix impede dislocation slip, thereby increasing strength. Therefore, fine-grain strengthening and second-phase strengthening are the primary mechanisms contributing to the high strength of the extruded AM80EA alloy.

5. Conclusions

In this study, extruded Mg-Al-Mn-Ce-(Ca) alloy profiles with novel comprehensive mechanical properties were fabricated via the optimization of the composition design and the control of the extrusion process. Furthermore, the relationship between microstructure and mechanical properties was also investigated, and the following are the main conclusions:

(1) Through the composition design, high quality Mg-8Al-0.57Mn-0.42Ce-(0.31Ca) alloy profiles were successfully prepared, and a high YS of 190 MPa, UTS of 346 MPa, and high EL of 16% were achieved.

(2) Due to the precipitation of high-density micro-nano second phases in the extruded alloy profile, the AM80EA alloy obtains a finer grain size (average grain size of 6.96 μm), as compared with that of the AM80E alloy. Therefore, the precipitation strengthening and grain refinement strengthening together contribute to the high YS of the AM80EA alloy.

Author Contributions: Conceptualization, H.P. and G.Q.; methodology, W.L. and S.L.; software, Y.Z. and Z.P.; validation, Z.P., S.W. and Y.Z.; formal analysis, S.W. and S.L.; investigation, W.L. and H.P.; resources, W.L. and S.L.; data curation, W.L.; writing—original draft preparation, W.L. and H.P.; writing—review and editing, H.P.; visualization, H.P. and Y.R.; supervision, H.P., G.Q. and Y.R.; project administration, H.P. and Y.R.; funding acquisition, H.P. and G.Q. All authors have read and agreed to the published version of the manuscript.

Funding: We would like to thank the National Key Research and Development Program of China (2023YFB3710903), National Natural Science Foundation of China (No. U2167213), the Fundamental Research Funds for the Central Universities (N2202020) and XingLiao Talent Plan (XLYC2203202) for their financial support.

Data Availability Statement: The raw data supporting the conclusions of this article will be made available by the authors on request.

Conflicts of Interest: The authors declare that they have no known competing financial interests or personal relationships that could have appeared to influence the work reported in this paper.

Abbreviations

The following abbreviations are used in this manuscript:

AM80E	Mg-8al-0.57mn-0.42ce
AM80EA	Mg-8al-0.57mn-0.42ce-0.31ca
YS	Yield strength
UTS	Ultimate tensile strength
EL	Elongation
RE	Rare-earth
LRE	Light rare-earth
Ce	Cerium
Sm	Samarium
LAGBs	Low-angle grain boundaries
ED	Extrusion direction
OM	Optical microscopy
SEM	Scanning electron microscopy
EBSD	Electron backscatter diffraction
TEM	Transmission electron microscopy

References

1. Emadi, P.; Andilab, B.; Ravindran, C. Engineering lightweight aluminum and magnesium alloys for a sustainable future. *J. Indian Inst. Sci.* **2022**, *102*, 405–420.
2. Li, Y.Q.; Li, F.; Kang, F.W.; Du, H.Q.; Chen, Z.Y. Recent research and advances in extrusion forming of magnesium alloys: A review. *J. Alloys Compd.* **2023**, *953*, 170080.
3. Liu, B.; Yang, J.; Zhang, X.; Yang, Q.; Zhang, J.; Li, X. Development and application of magnesium alloy parts for automotive OEMs: A review. *J. Magnes. Alloy.* **2023**, *11*, 15–47. [CrossRef]
4. Song, J.; She, J.; Chen, D.; Pan, F. Latest research advances on magnesium and magnesium alloys worldwide. *J. Magnes. Alloy.* **2020**, *8*, 1–41. [CrossRef]
5. Jiang, H.; Yang, B.; Wu, Y.; Peng, B.; He, M. Deformation Behaviors and Microstructure Evolution of Mg-Zn-Y-Zr Alloys During Hot Compression Process. *Metals* **2024**, *14*, 1332. [CrossRef]
6. Su, N.; Wu, Q.; Ding, C.; Wu, Y.; Peng, L. Effect of Y and Gd solutes on grain refinement of the as-extruded Mg-Gd (-Y)-Zn-Mn alloys. *J. Alloys Compd.* **2023**, *968*, 171804.
7. Zheng, Z.; Dong, Z.; Jiang, B.; Cheng, Y.; Zhang, A.; Song, J.; Li, T.; Pan, F. Evolution of strength with rare-earth content in highly-alloyed Mg-Gd-Y alloys. *Scr. Mater.* **2024**, *238*, 115772.
8. Che, C.; Cai, Z.; Cheng, L.; Meng, F.; Yang, Z. The Microstructures and Tensile Properties of As-Extruded Mg–4Sm–xZn–0.5Zr (x = 0, 1, 2, 3, 4 wt%) Alloys. *Metals* **2017**, *7*, 281.
9. Gensch, F.; Gall, S.; Lechner, S.; Fahrenson, C.; Mueller, S. Microstructural Stability of Extruded Mg-Mn-Ce Hollow Profiles with Weld Seams. *Metals* **2021**, *11*, 547. [CrossRef]

10. Mao, H.; Bai, X.; Wang, Y.; Xu, H.; Hou, J.; Wei, L.; Misra, R.D.K. Microstructures and High-Temperature Properties of Sm-Modified Mg-4Al-4RE Alloy. *Metals* **2022**, *12*, 135. [CrossRef]
11. Li, J.; Xie, D.; Zeng, Z.; Song, B.; Xie, H.; Pei, R.; Pan, H.; Ren, Y.; Qin, G. Mechanistic investigation on Ce addition in tuning recrystallization behavior and mechanical property of Mg alloy. *J. Mater. Sci. Technol.* **2023**, *132*, 1–17. [CrossRef]
12. Xie, D.; Pan, H.; Pan, Z.; Fu, T.; Zeng, Z.; Xie, H.; Ren, Y.; Tang, W.; Qin, G. Achieving outstanding heat-resistant properties in Mg alloy via constructing stable solute-network. *Mater. Res. Lett.* **2023**, *11*, 374–382. [CrossRef]
13. Kondori, B.; Mahmudi, R. Effect of Ca additions on the microstructure, thermal stability and mechanical properties of a cast AM60 magnesium alloy. *Mater. Sci. Eng. A* **2010**, *527*, 2014–2021.
14. Zha, M.; Wang, S.C.; Jia, H.L.; Yang, Y.; Ma, P.K.; Wang, H.Y. Effect of minor Ca addition on microstructure and mechanical properties of a low-alloyed Mg–Al–Zn–Sn alloy. *Mater. Sci. Eng. A* **2023**, *862*, 144457.
15. Zhang, W.; Shen, Z.; Pan, H.; Wang, T.; Fu, T.; Xie, D.; Tang, A.; Teng, C.; Wu, L.; Qin, G. Enhancing strength and irradiation tolerance of Mg alloy via co-addition of Mn and Ca elements. *J. Mater. Sci. Technol.* **2025**, *216*, 38–51.
16. Pan, H.; Qin, G.; Xu, M.; Fu, H.; Ren, Y.; Pan, F.; Gao, Z.; Zhao, C.; Yang, Q.; She, J.; et al. Enhancing mechanical properties of Mg–Sn alloys by combining addition of Ca and Zn. *Mater. Des.* **2015**, *83*, 736–744.
17. Zhang, J.; Peng, P.; Yang, Q.; Luo, A.A. Bimodal grain structure formation and strengthening mechanisms in Mg-Mn-Al-Ca extrusion alloys. *J. Magnes. Alloy.* **2023**, *11*, 4407–4419.
18. Akbaripanah, F.; Fereshteh-Saniee, F.; Mahmudi, R.; Kim, H. Microstructural homogeneity, texture, tensile and shear behavior of AM60 magnesium alloy produced by extrusion and equal channel angular pressing. *Mater. Des.* **2013**, *43*, 31–39. [CrossRef]
19. Cheng, R.; Li, M.; Du, S.; Pan, H.; Liu, Y.; Gao, M.; Zhang, X.; Huang, Q.; Yang, C.; Ma, L.; et al. Effects of single-pass large-strain rolling on microstructure and mechanical properties of Mg-Al-Ca alloy sheet. *Mater. Sci. Eng. A* **2020**, *786*, 139332. [CrossRef]
20. Huang, W.; Chen, J.; Jiang, Z.; Xiong, X.; Qiu, W.; Chen, J.; Ren, X.; Lu, L. Influence of Ca Content on Microstructure and Mechanical Properties of Extruded Mg–Al–Ca–Mn Alloys. *Acta Metall. Sin.* **2022**, *36*, 426–438. [CrossRef]
21. Huang, X.; Suzuki, K.; Chino, Y.; Mabuchi, M. Influence of aluminum content on the texture and sheet formability of AM series magnesium alloys. *Mater. Sci. Eng. A* **2015**, *633*, 144–153. [CrossRef]
22. Mert, F.; Akar, N.; Kilicli, V. Influence of Cerium Addition on Microstructure, Mechanical Properties, and Dry Sliding Wear Behavior of AM50 Magnesium Alloy. *Int. J. Met.* **2024**. [CrossRef]
23. Nakata, T.; Xu, C.; Ajima, R.; Shimizu, K.; Hanaki, S.; Sasaki, T.; Ma, L.; Hono, K.; Kamado, S. Strong and ductile age-hardening Mg-Al-Ca-Mn alloy that can be extruded as fast as aluminum alloys. *Acta Mater.* **2017**, *130*, 261–270. [CrossRef]
24. Park, S.H.; Kim, S.-H.; Kim, Y.M.; You, B.S. Improving mechanical properties of extruded Mg–Al alloy with a bimodal grain structure through alloying addition. *J. Alloys Compd.* **2015**, *646*, 932–936. [CrossRef]
25. Razzaghi, M.; Mirzadeh, H.; Emamy, M. Mechanical properties of Mg-Al-Mn magnesium alloys with low Al content in the as-cast and extruded conditions. *Mater. Res. Express* **2019**, *6*, 106521. [CrossRef]
26. Zhang, L.; Deng, K.-K.; Nie, K.-B.; Xu, F.-J.; Su, K.; Liang, W. Microstructures and mechanical properties of Mg–Al–Ca alloys affected by Ca/Al ratio. *Mater. Sci. Eng. A* **2015**, *636*, 279–288. [CrossRef]
27. Gao, W.; Wang, X.; Lin, Y.; Wang, X.; Liu, D.; Sun, X. Achieving ultra-high strength and ductility in a rare-earth-free magnesium alloy via precisely controlled secondary hot extrusion process with an extremely low extrusion speed. *J. Magnes. Alloy.* **2024**, *12*, 5216–5230. [CrossRef]
28. Luo, Y.-X.; Dong, B.-X.; Yang, H.-Y.; Qiu, F.; Yan, B.-C.; Shu, S.-L.; Jiang, Q.-C.; Shi, F.-J. Research progress on nanoparticles reinforced magnesium alloys. *J. Mater. Res. Technol.* **2024**, *30*, 5166–5191. [CrossRef]
29. Chen, Q.; Chen, R.; Su, J.; He, Q.; Tan, B.; Xu, C.; Huang, X.; Dai, Q.; Lu, J. The mechanisms of grain growth of Mg alloys: A review. *J. Magnes. Alloy.* **2022**, *10*, 2384–2397. [CrossRef]
30. Zhang, Z.; Zhang, J.; Wang, J.; Li, Z.; Xie, J.; Liu, S.; Guan, K.; Wu, R. Toward the development of Mg alloys with simultaneously improved strength and ductili-ty by refining grain size via the deformation process. *Int. J. Miner. Metall. Mater.* **2021**, *28*, 30–45. [CrossRef]
31. Yu, H.; Xin, Y.; Wang, M.; Liu, Q. Hall-Petch relationship in Mg alloys: A review. *J. Mater. Sci. Technol.* **2018**, *34*, 248–256.
32. He, S.-h.; Wang, C.; Sun, C.; Zhang, Y.; Yan, K.; Jiang, J.-h.; Bai, J.; Xue, F.; Liu, H. Corrosion properties of ECAP-processed Mg–Al–Ca–Mn alloys with separate Al_2Ca and Mg_2Ca phases. *Trans. Nonferrous Met. Soc. China* **2022**, *32*, 2527–2540.
33. Luo, S.; Wang, L.; Wang, J.; Zhu, G.; Zeng, X. Micro-compression of Al_2Ca particles in a Mg-Al-Ca alloy. *Materialia* **2022**, *21*, 101300.
34. Zhan, H.; Zhang, J.; Miao, J.; Wang, C.; Zeng, G.; Wang, J.; Luo, A.A. A low-cost Mg–Al–Mn–Zn alloy for automotive road wheel applications. *Mater. Sci. Eng. A* **2024**, *897*, 146321.

Disclaimer/Publisher's Note: The statements, opinions and data contained in all publications are solely those of the individual author(s) and contributor(s) and not of MDPI and/or the editor(s). MDPI and/or the editor(s) disclaim responsibility for any injury to people or property resulting from any ideas, methods, instructions or products referred to in the content.